Numerical study of flow and heat transfer in the vapour grooves of a loop heat pipe evaporator

Pierre-Yves Fravallo, Marc Prat, Vincent Platel

Numerical study of flow and heat transfer in the vapour grooves of a loop heat pipe evaporator

Pierre-Yves FRAVALLO[1], Marc PRAT[1], Vincent PLATEL[2]

[1]*Institut de Mécanique des Fluides de Toulouse (IMFT), Université de Toulouse, CNRS – Toulouse, France*

[2]*Univ. Pau & Pays Adour / E2S UPPA, Laboratoire de Thermique, Energétique et Procédés-IPRA EA1932, 64000, Pau, France*

Corresponding author: mprat@imft.fr

Abstract

A three-dimensional numerical study is developed to investigate the heat and mass transfer in the vapour removal channels of a Loop Heat Pipe (LHP). The heat transfer governing equations and the Navier-Stokes equations are solved under steady-state conditions for two vapour removal channel configurations: when the channels are in the wick and when the channels are in the casing. The boundary conditions for both configurations are extracted from numerical simulations using a model of the evaporator in which the modelization of the transfers in the wick is based on a pore network model. The results show that assuming that the vapour temperature in the channels is close to the saturation temperature is acceptable when the channels are within the wick but questionable when the vapour removal channels are within the casing. The simulations also indicate significant variations of the wall temperature between the various channel limiting surfaces. The heat transfer coefficient is different on the various surfaces and cannot be predicted using standard correlations for convective heat transfer in pipes.

Keywords: Two-phase cooling systems; Loop Heat Pipe; Numerical simulations; Convective heat transfer coefficient; Porous media;

Nomenclature

AR	Aspect Ratio
C_{pv}	Specific heat capacity, J/kg/K
D_H	Hydraulic diameter, m
h	Convective heat transfer coefficient, W/m^2/K
h_{lv}	Latent heat of vaporization, J/kg
$L_x, L_y, L_z,$ L_{xv}, L_{yg}, L_{yw}	Geometrical dimensions, m
$\dot{m}$	Mass flow rate, kg/s
M	Molar mass, g/mol
n	Unit normal vector
P	Pressure, Pa
$Per.$	Perimeter, m
R	Ideal gas constant, J/kg/K
S	Surface area, m^2
T	Temperature, K
T_{sat}	Saturation temperature, K
U	Velocity vector, m/s
u_{inj}	Injection velocity, m/s

Greek symbols

λ	Thermal conductivity, W/m/K
μ	Dynamic viscosity, Pa s
ν	Kinematic viscosity, m^2/s
φ	Heat flux (W/m^2)
ρ	Density, kg/m^3

Dimensionless number

Nu	Nusselt number
Pr	Prandtl number
$\Re$	Reynolds number

Subscripts

c	convective
CC	Compensation chamber
$inj.$	Injection
sat	Saturation
v	Vapour

1.Introduction

With the miniaturization of electronic components and the increasing required power, the thermal control of electronic devices is a crucial issue. In this context, capillary pumped loops (CPLs) and loop heat pipes (LHPs) are very efficient systems to dissipate high heat fluxes over a large distance. First developed for spatial applications, this type of cooling device is now also considered for terrestrial applications such as automobile or railway transport [1-4]. CPLs and LHPs are diphasic thermal control devices based on a vaporization – condensation process of a working fluid to transfer the heat. One can refer for example to [5] for a comparative discussion of both systems. In what follows, a LHP is more specifically considered but the results presented later in the paper apply to both systems. As sketched in Fig.1, a LHP is composed of an evaporator connected to the condenser through a vapour line, a liquid line between the condenser and the reservoir which is itself connected to the evaporator. The evaporator is made of a metallic casing in contact with a porous wick sucking the fluid by capillarity. The vapour forming in the evaporator is collected in vapour removal channels, referred to as vapour grooves in what follows, and exits the evaporator in the vapour line.

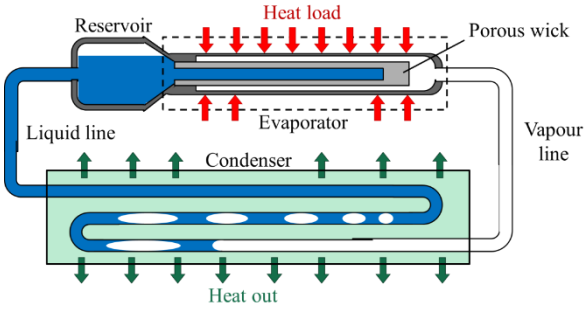

Fig.1-Sketch of a loop heat pipe (figure from [18])

The grooves are typically straight channels of rectangular cross-section machined either in the casing or the porous wick. Fig.2 shows the schematic cross-section of a flat evaporator for both groove configurations.

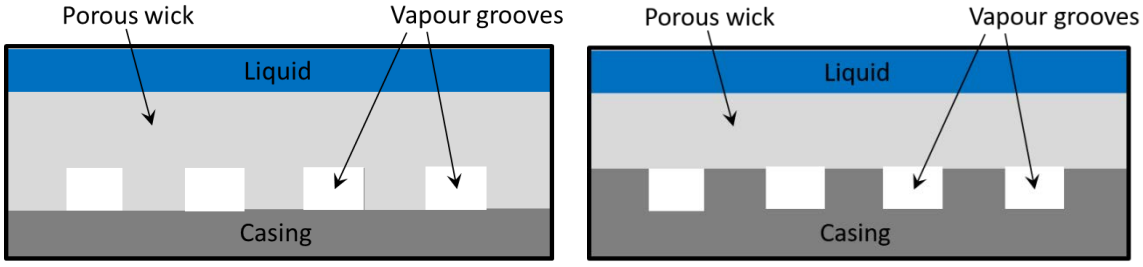

Fig.2 - Schematic of a flat evaporator cross-section with the vapour grooves in the wick (left) or in the casing (right).

LHPs have been the subject of many experimental and/or numerical studies and is still a very active research topic, e.g. [6-15] to mention only a series of recent works. One can refer to [16-17] for literature reviews. As discussed in [18], one can distinguish two main investigation scales. The first one is the whole loop. At this scale, modelling of transfers in each LHP component is typically performed via a simplified 0D or 1D approach, e.g. [19-21]. The second category of models aims at developing detailed modelling of the transfers at the scale of a component or a sub-region of the component. The 3D simulations in an evaporator element presented in [18; 22-24] are representative of this type of approach. At this scale, the heat and mass transfer problem in the evaporator can be seen as a conjugate heat and mass transfer problem between the various components of the evaporator, namely the casing, the porous wick, the grooves, the liquid line connecting the evaporator to the reservoir (also referred to as the compensation chamber (CC)). A detailed modelling approach then requires to compute the flow in the grooves and the liquid line in the evaporator by solving the Navier-Stokes equations and the heat transfer equation coupled with a model describing the heat and mass transfer in the porous wick and the heat transfer in the casing. To the best of our knowledge, such a complete 3D numerical approach has not yet been developed. In [22], the 3D flow in the groove was computed but only the regime where the wick is fully saturated was considered. A somewhat similar approach was considered in [23] again considering the wick as fully saturated. A difference between these two studies lies in the position of the groove: in the casing in [22] and in the wick in [23]. As discussed in [18], the regime where the wick is fully saturated corresponds to low heat loads and therefore is not representative of the LHP nominal operating conditions. According to [18], the wick is partially invaded by the vapour under the nominal conditions. This corresponds to a situation where the wick at the wick-groove interface is partially saturated with coexistence of pores filled by the liquid and of pores filled by the vapour. The detailed simulations of the liquid–vapour distribution in the wick reported in [18] were based on a pore network approach in which the pore space is represented as a network of pore bodies connected by narrower conduits referred to as throats. However, the modelling of the conjugate transfers between the pore network model (PNM) and the grooves and between the casing and the grooves was simplified assuming that the temperature in the grooves was the saturation temperature and using the correlation proposed in [25] for the computation of the convective heat transfer in the grooves. This correlation was also used in [26] in a numerical study of heat and mass transfer in a LHP evaporator. Thus, the heat transfer and momentum equations were not explicitly solved in the vapour grooves. Also, the temperature and pressure in the grooves were assumed to be constant along the grooves. In this context, the objective of the present study is to explore whether these simplifications are acceptable. In other words, the objective is to make a step forward toward more comprehensive and accurate simulations through detailed computations of the heat and mass transfer in the grooves for both cases, i.e. when the grooves are in the wick and when the grooves are machined in the casing. The literature is scarce on this topic. To the best of

our knowledge, the most detailed investigation is the study presented in the Ph.D thesis by Jesuthasan [27]. However, only the case of the grooves in the casing was considered and the temperature of the groove–casing limiting surface was assumed to be spatially uniform and identical on each wall. Also, the vapour injection velocity at the wick-groove interface was assumed spatially uniform. The simulations presented in [18] indicate that these features are questionable simplifications. In order to consider more representative conditions, the boundary conditions for the computation of the heat and mass transfer in the groove are obtained in the present study from numerical simulations over an evaporator unit cell using the model presented in [18].

In addition to a contribution to the CPL / LHP study, the work presented in this paper can be also seen as an extension of the works devoted to the analysis of the effects of blowing (injection) from the wall on heat transfer and pressure losses in laminar channel flows, e.g. [28-29].

The paper is organized as follows. The model of heat and mass transfer in the groove for both cases is presented in section 2. The method to specify the boundary conditions from simulations using the model presented in [18] is presented in section 3 together with the input data required for the groove heat and mass transfer simulations. The main results are presented in section 4. A short discussion is presented in section 5. Conclusions are given in section 6.

2. Modelling of fluid flow and heat and mass transfer in vapour groove

The computational domains considered in the present study are displayed in Fig.3 for the case of the grooves in the wick and in Fig.4 for the case of the grooves is in the casing. Because of the symmetry about the lateral planes (surfaces 3 and 10 in Fig.3, surfaces 3 and 9 in Fig.4), only a half groove and a half casing (in the x-direction) are considered.

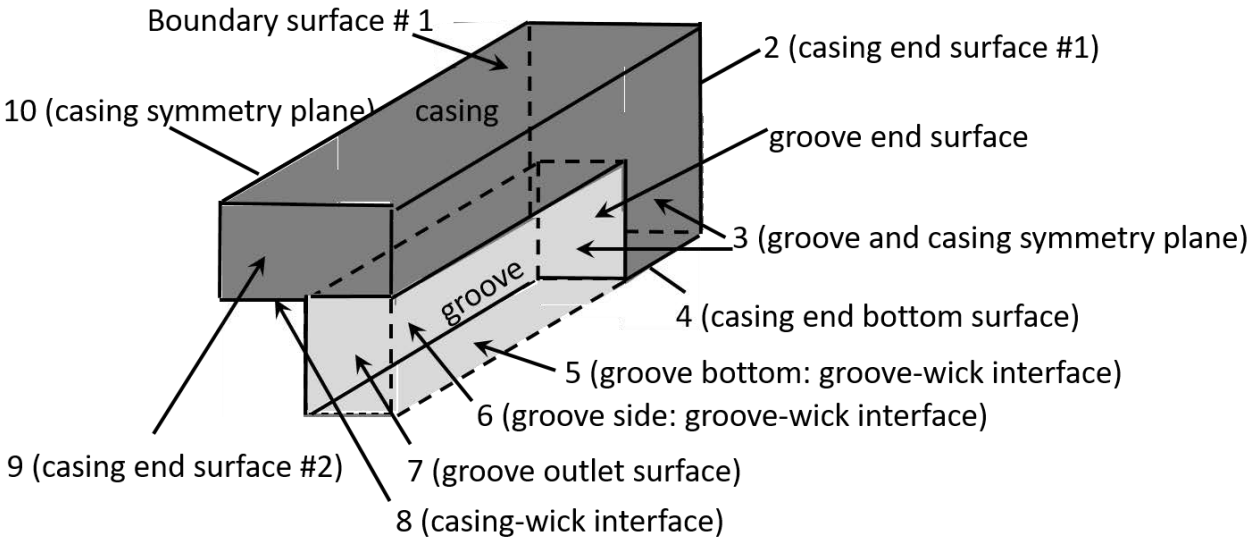

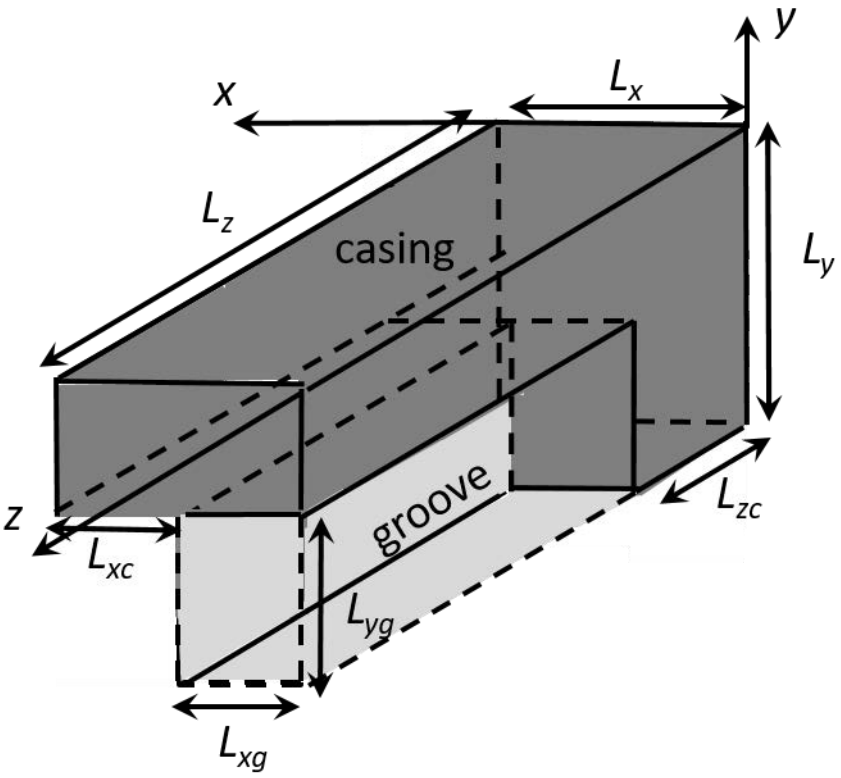

Fig.3 -Sketch of computational domain for the case of the vapour grooves in the wick.

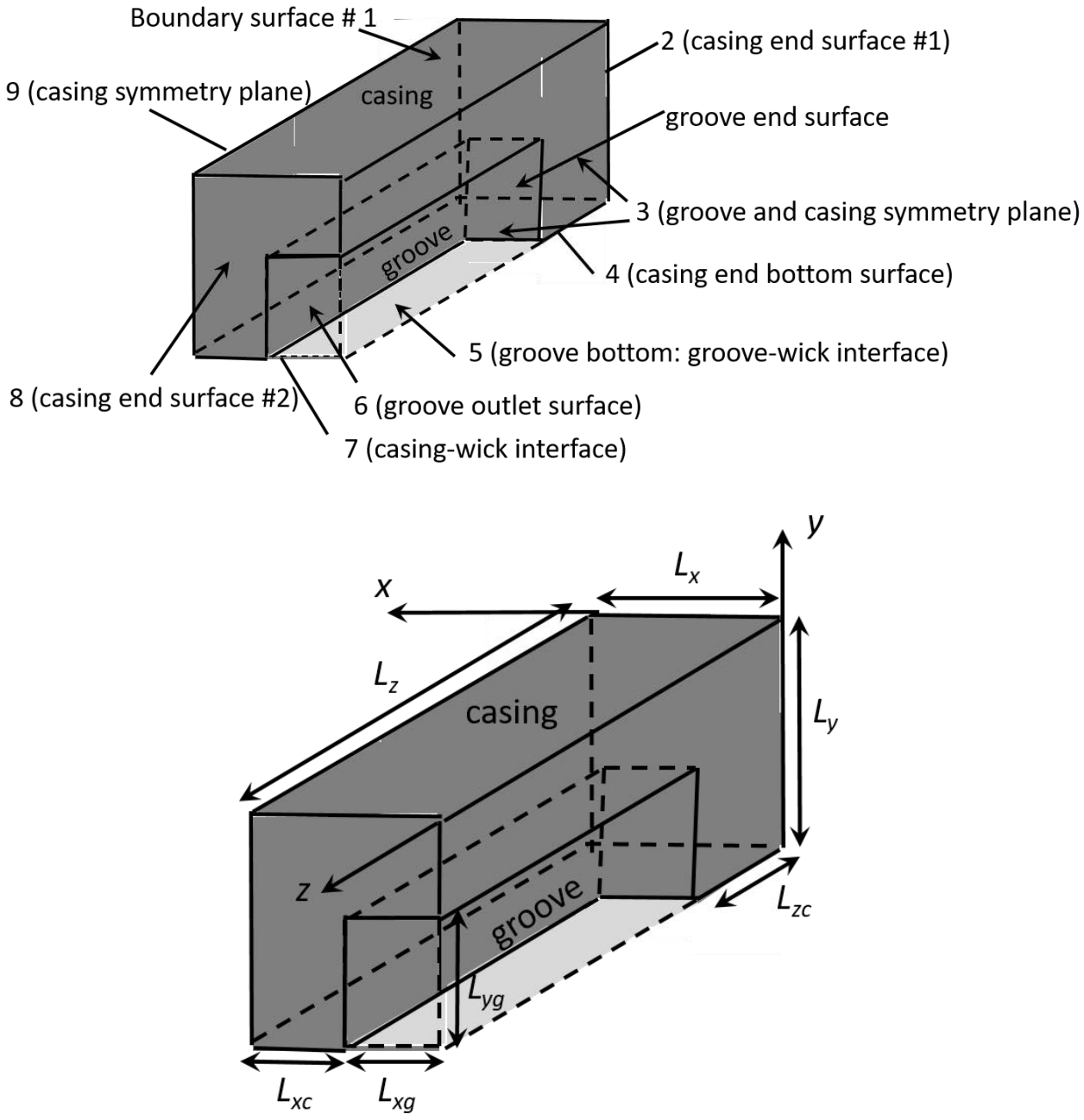

Fig.4 - Sketch of computational domain for the case of the vapour grooves in the casing.

The corresponding geometrical dimensions are reported in Table 1.

Table 1 - Geometrical dimensions of computational domains shown in Fig.3 and 4.

Groove in casing and groove in wick	
L_x (mm)	0.95
L_{xc} (mm)	0.125
L_{xg} (mm)	0.35
L_{yg} (mm)	0.7
L_y (mm)	1.7
L_z (mm)	100.5
L_{zc} (mm)	0.5

As indicated in Table 1, the groove length is 10 cm, which is representative of grooves in LHP evaporators. Since grooves are symmetrical about their longitudinal vertical middle plane, computations are performed over a half groove. Note also that the computational domain include the dead-end limiting surface of the groove (groove end surface in Figs. 3 and 4). As can be seen from Figs.3 and 4, the groove is closed at this end by the casing. Note also that the heat leak between the groove and the compensation chamber through the casing is taken into account (heat leak through the casing wall closing the groove at one end).

2.1 Governing equations

Influence of gravity is neglected as well as the impact of viscous dissipation on heat transfer. All thermophysical properties are considered constant except for the vapour density which is computed using the ideal gas law. The working fluid is ammonia. Steady states are considered. The mathematical formulation of the considered problem is now presented.

Heat conduction in the casing

The heat transfer governing equation in the casing reads

$$\nabla.\left(\lambda_{casing}\nabla T\right) = 0 \tag{1}$$

where T is the temperature and λ_{casing} is the casing thermal conductivity. The casing is assumed to be in stainless steel (λ_{casing} = 16.3 W m^{-1} K^{-1})

Heat Transfer in the groove

Because of the fluid flow inside the groove, the heat transfer occurs through conduction and forced convection

$$\left(\rho_v C_{pv} U\right).\nabla T = \nabla.(\lambda_v \nabla T) \tag{2}$$

where $\rho_v$is the vapour density computed using the ideal gas law, $\rho_v = \frac{p}{MRT}$, where p is the vapour pressure, M is the vapour molecular weight, R is the universal gas constant; C_{pv} is the vapour heat capacity (C_{pv} =2841.3 J K^{-1} kg^{-1}), λ_v is the vapour thermal conductivity 0.024 W m^{-1} K^{-1}) and **U** is the vapour velocity vector.

Flow in the groove

The pressure and velocity fields in the groove are computed solving the continuity and Navier-Stokes equations,

$$\nabla.(\rho_v U) = 0 \tag{3}$$

$$\rho_v(U.\nabla U) = \nabla.\left(-pI + \mu_v(\nabla U + (\nabla U)^T) - \frac{2}{3}\mu_v(\nabla.U)I\right) \tag{4}$$

where **I** is the identity matrix and μ_v is the vapour dynamic viscosity (μ_v =9.63 x 10^{-6} Pa s).

2.2 Boundary conditions

The boundary conditions are specified considering separately the two cases: groove in the casing and groove in the wick. The numbers refer to the numbering of boundary surfaces in Fig.3 (groove in the wick) and Fig.4 (groove in the casing).

Groove in the wick

The boundary surface numbering is given in Fig.3.

-Top of the Casing (boundary surface #1)

$$T = T_{casing} \tag{5}$$

As detailed in section 3, T_{casing} is obtained from PNM simulations.

-Casing limiting surface in contact with Compensation Chamber (boundary surface #2),

$$\lambda_{casing}\nabla T.n = \frac{\lambda_{casing}\left(T_{sat_{CC}} - T\right)}{L_{zc}} \tag{6}$$

Where n is a unit vector normal to the considered surface, L_{zc} is the half thickness of the casing region between the groove dead-end surface and the compensation chamber (L_{zc} = 0.5 mm), and $T_{sat_{CC}}$ is the temperature in the compensation chamber ($T_{sat_{CC}}$= 283.15 K). In this approach, only one half of the casing region in contact with the compensation chamber is taken into account in the 3D simulation whereas the second half is taken into account through the BC Eq.(6). Actually, although this reduces a bit the computational domain, it would

have been simpler to consider the whole region and impose the temperature in the CC as boundary condition. However, since the thermal conductivity of the casing is high, the latter option should lead to results very similar to the ones presented in the article.

-Groove and casing symmetry surface at $x = 0$ (boundary surface #3):

$$\nabla T.n = 0 \tag{7}$$

In addition, the vapour velocity component normal to this groove limiting surface is imposed to zero,

$$U.n = 0 \tag{8}$$

Symmetry conditions are imposed as regards the two other components of the velocity vector.

-Casing bottom limiting surface at the beginning of evaporator (boundary surface #4):
This temperature cannot be obtained from the PNM simulations. The temperature at this interface is assumed to be close to the saturation temperature since this surface is between the compensation chamber and the wick-groove bottom interface, which are both to temperatures close to the saturation temperature.

$$T = T_{sat_{CC}} \tag{9}$$

-Wick-groove bottom interface (boundary surface # 5):
The temperature at this interface is assumed to be close to the saturation temperature since the PNM simulations reported in [18] show that this interface remains highly liquid saturated.

$$T = T_{sat_{CC}} \tag{10}$$

$$U.n = u_{inj-bottom}(x) \tag{11}$$

where u_{inj} is the injection velocity resulting from the vaporization of the liquid within the wick or at its surface. As detailed in section 3, u_{inj} is obtained from PNM simulations. A no-slip condition is used as regards the velocity components parallel to the considered interface.

- Wick-groove side interface (boundary surface #6)
The temperature at this interface is assumed to be close to the saturation temperature since the PNM simulations reported in [18] show that this interface remains highly liquid saturated.

$$T = T_{sat_{CC}} \tag{12}$$

The velocity normal component is specified as

$$U.n = u_{inj-side}(y) \tag{13}$$

-Groove outlet (boundary surface # 7):
An outflow condition is applied,

$$\lambda_v \nabla T.n = 0 \tag{14}$$

whereas a no stress condition is chosen for the flow:

$$\left(-pI + \mu_v(\nabla U + (\nabla U)^T) - \frac{2}{3}\mu_v(\nabla.U)I\right).n = 0 \tag{15}$$

-Wick-casing interface (boundary surface #8):
As detailed in Section 3, the temperature distribution at this interface is obtained from PNM simulations and is therefore an input data for the heat and mass transfer simulations in the groove,

$$T = T_{wickcasing}(x) \tag{16}$$

- Casing end surface #2 (boundary surface # 9)
The following condition is applied on this surface

$$\lambda_{casing} \nabla T.n = 0 \tag{17}$$

-Casing second lateral face (boundary surface # 10):

$$\nabla T.n = 0 \tag{18}$$

-Casing end-wick vertical limiting surface (boundary surface #11, not visible in Fig. 3):
As explained in the next section, the conditions at this interface cannot be imported from the simulations performed to obtain the boundary condition missing information. For simplicity, a no heat flux condition is imposed

$$\nabla T.n = 0 \tag{19}$$

Groove in the casing

Although many boundary conditions are identical for both cases, the corresponding boundary conditions are given again for clarity.

-Top of the Casing (boundary surface #1):

$$T = T_{casing} \tag{20}$$

-Casing limiting surface in contact with Compensation Chamber (boundary surface #2),

$$\lambda_{casing}\nabla T.n = \frac{\lambda_{casing}\left(T_{sat_{CC}} - T\right)}{L_{zc}} \tag{21}$$

-Groove and casing symmetry plane at $x = 0$ (boundary surface #3):

$$\nabla T.n = 0 \tag{22}$$

$$U.n = 0 \tag{23}$$

-Casing bottom limiting surface at the beginning of evaporator (boundary surface #4):

$$T = T_{sat_{CC}} \tag{24}$$

-Wick-groove bottom interface (boundary surface #5):

$$T = T_{sat_{CC}} \tag{25}$$

$$U.n = u_{inj-bottom} \tag{26}$$

-Groove outlet (boundary surface # 6):

$$\lambda_v \nabla T.n = 0 \tag{27}$$

$$\left(-pI + \mu_v(\nabla U + (\nabla U)^T) - \frac{2}{3}\mu_v(\nabla . U)I\right).n = 0 \tag{28}$$

-Wick-casing interface (boundary surface # 7):

$$T = T_{wickcasing}(x) \tag{29}$$

-Casing end surface adjacent to the vapor groove outlet (boundary surface #8):

$$\nabla T.n = 0 \tag{30}$$

-Casing second end surface (boundary surface # 8):

$$\nabla T.n = 0 \tag{31}$$

For the internal boundaries between casing and groove (groove end surface in Fig.4 and groove top surface - casing interface and groove side surface – casing interface) temperature and heat flux continuity and velocity wall conditions are applied.

3. Specification of boundary condition input data

To solve the above problems, several boundary conditions must be quantitatively specified, namely T_{casing}, $T_{wick-casing}(x)$, $u_{inj-side}(y)$, $u_{inj-bottom}(x)$. As mentioned in the introduction, the heat and mass transfer problem in the evaporator grooves is actually a conjugate heat and mass transfer problem in which the heat and mass transfer in the grooves is coupled with the transfers in the casing and the wick (and actually in the other components of the loop). In other words, one cannot specifyT_{casing}, $T_{wickcasing}(x)$, $u_{inj-side}(y)$ and $u_{inj-bottom}(x)$ independently from each other. They all depend on the applied heat flux on top of the casing.

In order to take into account this feature, the needed data were computed from simulations using the evaporator unit cell model presented in [18]. This model is referred to as the PNM (Pore Network Model) because a pore network model is used to compute the heat and mass transfer in the wick. The method with inputs from PNM simulations to compute the heat and mass transfer in the groove is summarized in Fig.5.

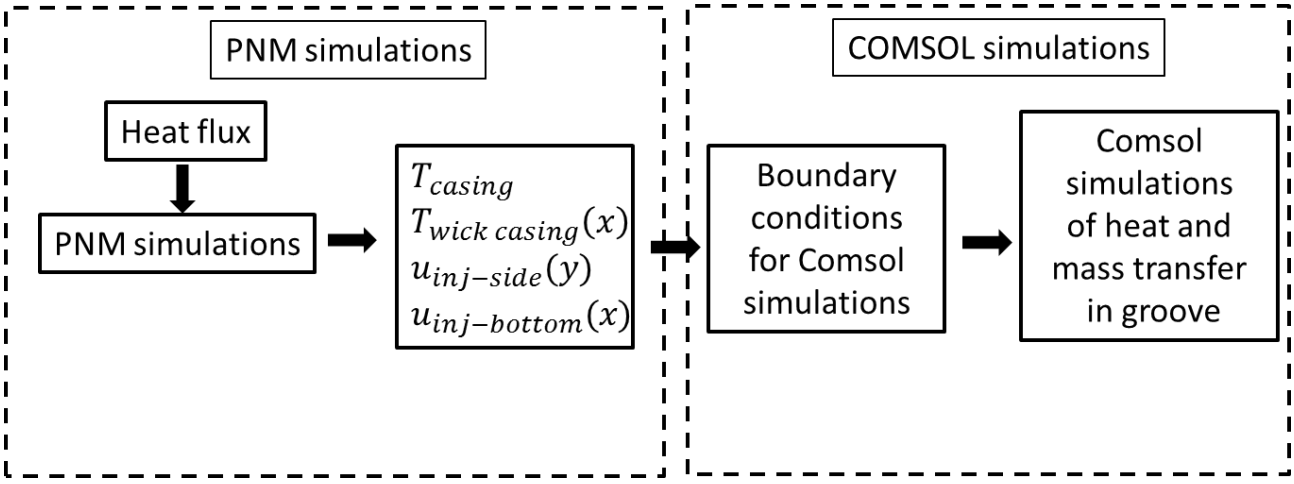

Fig.5 - Sketch of the one-way coupling method used to specify the boundary conditions needed to solve the heat and mass transfer problem in the groove.

3.1 Pore network modelling of evaporator unit cell

The PN Model and the associated numerical PNM code used in this study are the same ones as in [18]. Only the main features of direct interest for the present study are presented. Figure 6 shows a sketch of the PNM computational domain, which is referred to as a 3D unit cell, for both cases, i.e. when the grooves are in the wick and when the grooves are in the casing. The unit cell can be divided into 3 areas: the vapour grooves, the casing and the wick. Heat and mass transfers in both the liquid and vapour phases take place in the wick whereas heat conduction is considered in the casing. The lattice spacing, i.e. the distance between two pores,

is 61 µm. This corresponds to the mesh size used in the PNM computations. For the considered computational domains (Fig.6), which include the wick and the casing, the computational grid has about 50000 nodes (see [18] for the details). The conditions imposed in the vapour grooves are spatially uniform homogeneous conditions and are specified as follows.

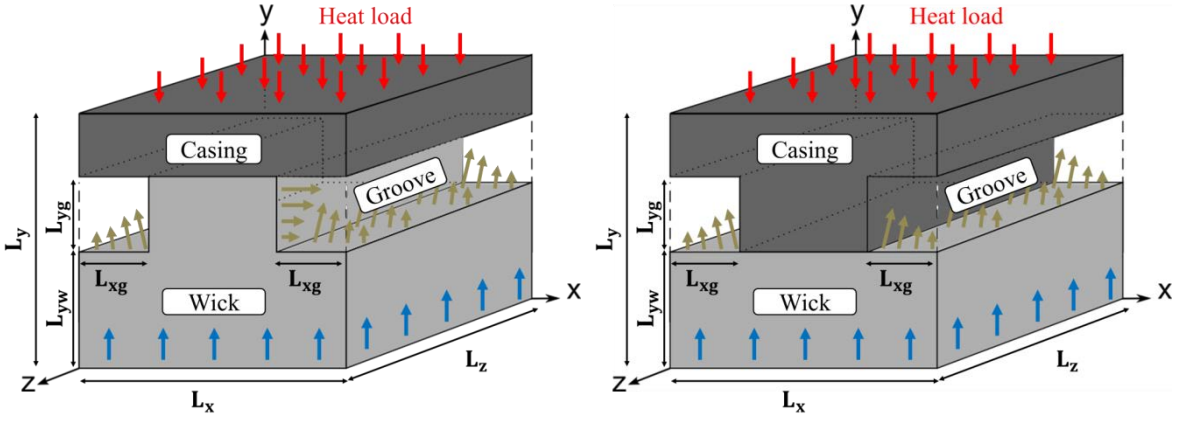

a) grooves in wick

b) grooves in casing

Fig.6 - Sketch of computational domains considered for the PNM simulations (figures from [18])

Conditions in the grooves

The groove temperature is computed using the Clausius-Clapeyron relationship from the saturation pressure ($P_{sat_{CC}}$) and temperature ($T_{sat_{CC}}$) in the compensation chamber (CC), which are input data for the model, as

$$T_{sat-grooves} = \left(\left(\frac{-R}{h_{lv}M}\left(ln\left(P_{grooves}\right) - ln\left(P_{sat_{CC}}\right)\right)\right) + \frac{1}{T_{sat_{CC}}}\right)^{-1} \tag{32}$$

where h_{lv} is the enthalpy of vaporization. The pressure $P_{grooves}$ in the grooves are the addition of pressure losses in grooves, pressure losses in the loop and pressure in the CC,

$$P_{grooves} = P_{sat_{CC}} + \Delta P_{Loop} + \Delta P_{grooves} \tag{33}$$

As explained in [18], the pressure lossesΔP_{Loop} in the elements of the loop elements (liquid line, condenser and vapour line) are computed using Poiseuille law. The pressure losses in the grooves is computed as in [18] using Eq. (33),

$$\Delta P_{grooves} = \frac{2\rho_v \nu_v \gamma \overline{U}_z L_z}{D_H^2} \tag{34}$$

whereD_H is the groove hydraulic diameter: $D_H = \frac{4S}{Per.} = \frac{8L_{xg}L_{yg}}{4L_{xg}+2L_{yg}}$, $\gamma = 4.7 + 19.64\left(\frac{AR^2+1}{(AR+1)^2}\right)$ where $AR = \frac{L_{yg}}{2L_{xg}}$.

The heat transfer convective coefficient $h_c$in the grooves is determined using the correlation proposed in [25],

$$Nu = \frac{h_c D_H}{\lambda_v} = 5 + 0.015\Re^a Pr^b \tag{35}$$

Where$\Re = \frac{\overline{U}_z \rho_v D_H}{\mu_v}$,$Pr\frac{Cp_v\mu_v}{\lambda_v}$,$a = 0.88 - \frac{0.24}{4} + Pr$ and $b = \frac{1}{3} + 0.5e^{-0.6Pr}$, $\overline{U}_z$ is the groove cross-section averaged axial vapour velocity.

Wick-groove interface

In order to determine the groove heat transfer coefficient from Eq.(35) as well as the saturation pressure and temperature in the groove, the average vapour velocity in the groove must be determined. This velocity is obtained from the total vaporization mass flow rate produced in the 3D unit cell. It is further assumed that this vaporization rate is about the same all along the groove. This leads to express the vapour average velocity at the groove exit as,

$$\overline{U}_z = \frac{\dot{m}_{tot}}{\rho_v 2L_{xg}L_{yg}} \frac{L_{evaporator}}{L_z} \tag{36}$$

where $\dot{m}_{tot}$is the total mass flow rate, i.e. the sum of the mass flow rate produced at the wick/groove interface from the pores in the liquid state and the mass flow rate produced at liquid-vapour interface within the wick. As indicated in Fig. 6; L_z is the length of the unit cell (Fig.6 and Table 2), $L_{evaporator}$ is the length of the evaporator (Table 2).

The method to compute the vapour-fluid flow and thermal transfer in the wick is detailed in [18]. The point of interest here is the thermal coupling between the wick and the groove which can be separated in two cases.

When the pore at the wick-groove interface is in the liquid state, i.e. occupied by the liquid, the interface temperature is imposed equal to the saturation temperature in the groove $T_{sat-grooves}$ (Eq.(32). When the pore is in the vapour state, a convective heat transfer boundary condition is applied as

$$\lambda_{vapour-wick}\nabla T.n = h_c\left(T - T_{sat-grooves}\right) \tag{37}$$

where the heat transfer coefficient h_c is computed using Eq.(35).

Casing - groove interface

As sketched in Fig.6, the heat flux is imposed over the casing top surface, spatially periodic boundary conditions are imposed on the lateral sides of the casing and a no flux condition is imposed on the side faces at $z = 0$ and $z = L_z$. At the casing-groove interface, the convective heat transfer condition is imposed,

$$\lambda_{casing} \nabla T . n = h_c \left(T - T_{sat-grooves} \right) \tag{38}$$

3.2 PNM simulation results

The PNM simulations were performed for the parameter values indicated in Table 2 for grooves in the casing or in the wick. The PNM is a discrete model in which the temperature and vapour velocity are computed in each pore of the wick. In contrast, the groove heat and mass transfer problem presented in section 2 is set according to a continuum framework. The commonly used procedure to produce continuous field from discrete field is volume averaging, e.g. [30] for an example. A somewhat similar procedure is used here by smoothing out the PNM data by performing spatial averages (as expressed by Eqs. (39-41) below).

Table 2 - PNM simulation parameters (notations refer to Fig.6)

Parameter	
Heat flux [W/m²]	1000 to 101000 by step of 5000
L_x [mm]	1.9
L_{xg} [mm]	0.35
L_y [mm]	3.4
L_{yw} [mm]	1.5
L_{yg} [mm]	0.7
L_z [mm]	2
$L_{evaporator}$ (mm)	100
Fluid	Ammonia
$P_{sat_{CC}}$ [Pa]	615050
$T_{sat_{CC}}$ [K]	283.15
Wick	Nickel
Casing	Stainless Steal

The maximal temperature on top of casing (Fig. 7) and the average temperature at the wick/casing interface (Fig. 8) are extracted from the pore network model simulations for each applied heat load for both cases.

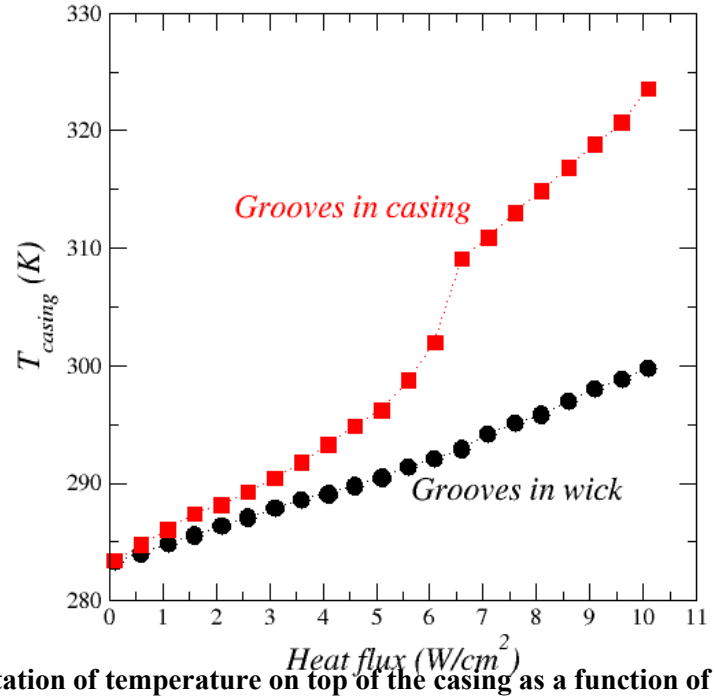

Fig. 7 - PNM computation of temperature on top of the casing as a function of heat flux for both cases

Note that the temperature is quite uniform over the casing top surface. The maximum temperature considered here is actually representative of the average temperature over the casing top surface. Fig.7 also illustrates the fact that setting the groove in the wick is more efficient since the casing top surface temperature is significantly lowerr when the groove is in the wick for a given heat flux.

$T_{wick-casing}(x)$ is obtained by averaging the temperature along the wick-casing interface. Using the coordinate system in Figs. 3 and 4, $T_{wick-casing}(x)$ is thus expressed as

$$T_{wick-casing}(x) = \frac{\int_{z=L_{zc}}^{z=L_z} T(x,-L_y,z)dz}{(L_z-L_{zc})} \tag{39}$$

Note that $x = 0$ corresponds in Figs.8 and 9 to the triple contact line between wick, groove and casing. This line is at $x = L_{xg}$ in Figs.3 and 4. In Figs. 8 and 9 the coordinate x rises up to the middle of the unit cell.

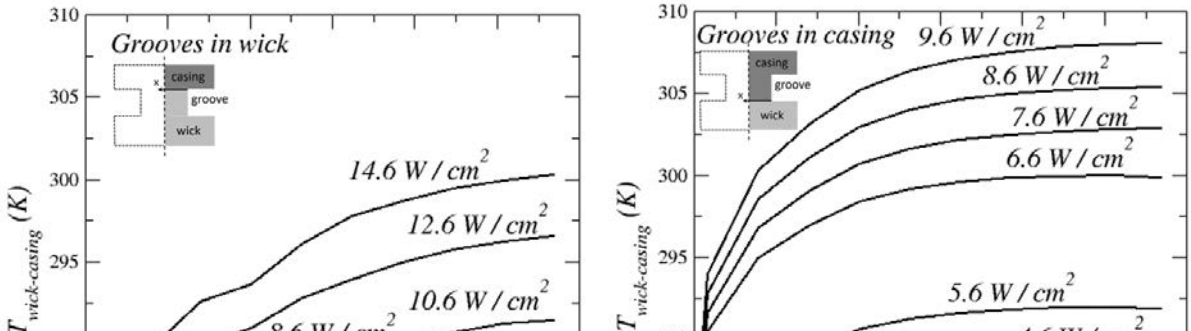

Fig. 8 - PNM computation of $T_{wick-casing}(x)$ (temperature at wick-casing interface) for the case of the grooves in the wick and the case of the grooves in the casing; x = 0 corresponds to the triple contact line wick–casing-groove interface.

As can be seen from Fig.8, the wick-casing temperature increases with the distance from the groove. The temperature is maximum in the middle of the rib formed either by the casing (groove in casing case) or the wick (groove in wick case). At a given location, $T_{wick-casing}(x)$ increases with the applied heat flux. As can be seen the variation of $T_{wick-casing}(x)$ with the heat flux is non-linear. The variation is more important for the higher heat fluxes and one can also see a jump in the temperature increase (between the heat fluxes 5.6 W/cm^2 and 6.6 W/cm^2 in Fig.8 right and between 10.6 W/cm^2 and 12.6 W/cm^2 in Fig.8 left). As discussed in [18] and sketched in Fig.9, three main evaporator operating regimes can be distinguished depending on the applied heat flux. For a sufficiently low heat flux, the wick is saturated and the vaporization takes place only at the wick surface. When the heat flux is sufficiently high, a two-phase zone takes place within the wick. The vapour and liquid phase coexists within a region of the wick and the vaporization takes place both with the wick and at its surface. When the heat flux is further increased, a dry zone eventually forms within the wick. The afore-mentioned temperature jumps correspond to the transition between regime II and regime III (sketched in Fig.9) when a vapour blanket starts forming in the wick The formation of the vapour blanket induces a higher resistance to heat transfer within the wick and consequently a comparatively higher increase in the casing temperature with an increasing heat flux.

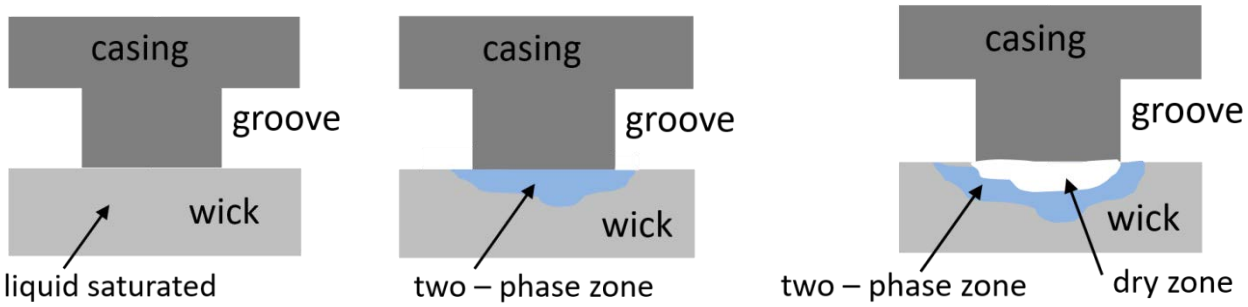

Regime I Regime II Regime III

Fig.9 - Schematic of the evaporator main operating regimes (illustrated for the groove in casing case).

The vapour injection velocity $u_{inj-bottom}(x)$ in the groove at the groove – wick bottom interface is depicted in Fig. 10. As expressed by Eq.(40), this velocity corresponds to the average velocity along longitudinal lines along the considered interface.

$$u_{inj-bottom}(x) = \frac{\int_{z=L_{zc}}^{z=L_z} u_v(x,y,z)dz}{(L_z - L_{zc})} \tag{40}$$

with $y = -L_y$ (Figs.3 and 4).

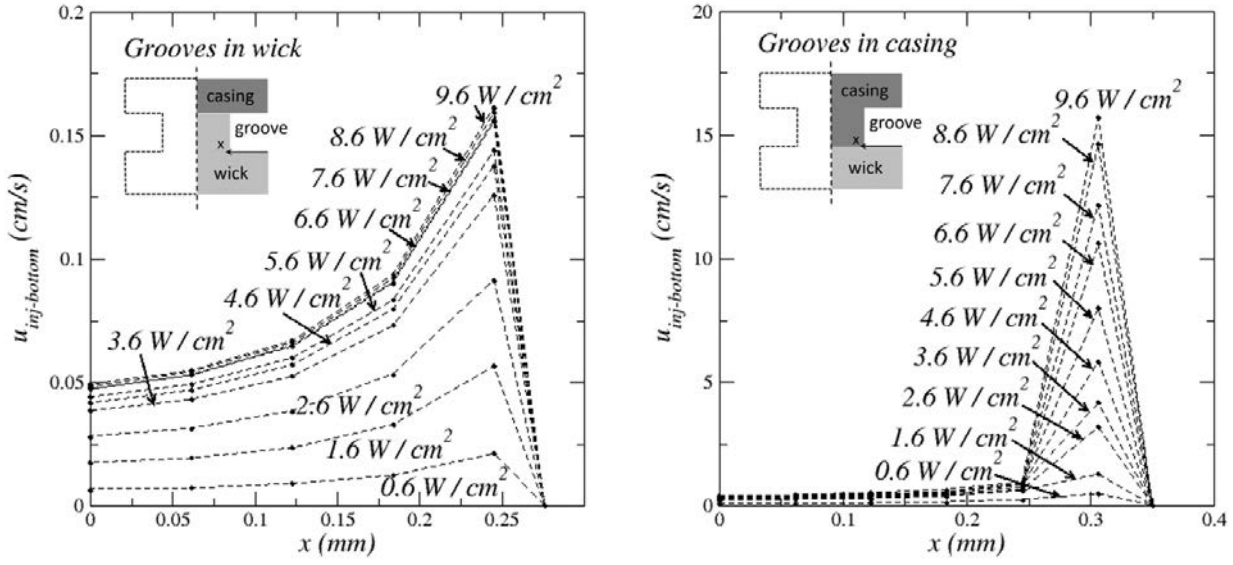

Fig.10 - PNM computation of$u_{inj-bottom}(x)$: vapour injection velocity at wick-groove interface for the case of the grooves in the wick and the case of the grooves in the casing for several heat fluxes; x = 0 corresponds to the middle of the groove.

Similarly, the injection velocity $u_{inj-side}(y)$ depicted in Fig. 11 is the average velocity along the groove as expressed by Eq.(41),

$$u_{inj-side}(y) = \frac{\int_{z=L_{zc}}^{z=L_z} u_v(x,y,z)dz}{(L_z - L_{zc})} \tag{41}$$

with $x = L_{xg}$ (Fig.3).

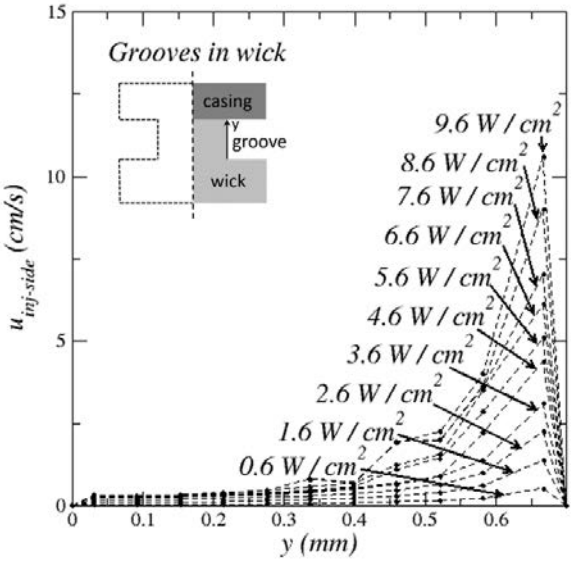

Fig.11 - PNM computation of$u_{inj-side}(y)$: vapour injection velocity at wick-groove lateral interface for groove in wick for several heat fluxes. In this figure, y = 0 corresponds to the intersection between the horizontal and vertical groove limiting surfaces as sketched in the figure.

As can be seen from Figs.10 and 11, the injection velocity varies significantly over the groove limiting surfaces. As regards the groove bottom surface, the injection velocity increases significantly in the region close to the casing (case of the grooves in the casing in Fig.10). This is because all the vapour forming in the region of the wick under the casing exits the wick in the region of the groove bottom surface close to the casing – wick –groove triple contact line. A somewhat similar situation can be observed when the groove is in the wick (Fig.10) with the greater velocities in the region close to the vertical groove-wick interfacial surface. However, the velocity magnitude is significantly lower when the grooves are in the wick compared to the case of the grooves within the casing. This is because the most active vaporization region inside the wick is under the casing. This is illustrated in Fig.11 for the groove side surface. The velocity increases in the region of the groove side surface close to the casing and the velocity magnitude is comparable to the one of the bottom

injection velocity for the case of the grooves in the casing in Fig.10. In summary, these figures well illustrate the fact that the injection velocity is not uniform over the groove-wick interfacial surfaces.

4. Results

In this section, the results of the 3D simulations of the vapour flow inside the vapour removal channel of a Loop Heat Pipe are presented and discussed. The first subsection is dedicated to the temperature behaviour, the second one to the pressure and then, in the last part, the convective heat transfer coefficient is discussed. To obtain these results, the simulations were performed with finite elements of variable sizes, smaller in the vicinity of the interfaces or boundaries. The mesh was adjusted through a series of test using a COMSOL relative tolerance criterion of 10^{-10}. For instance, for the case of the groove in the casing, this led to a mesh containing 2 824 778 elements. The size of the elements varied but was on average of the same order as the mesh size in the PNM simulations in the groove transverse directions, i.e. on the order of 60 µm. This means that there were about 12 elements over the width of the groove. Convergence was not possible or judged too long to achieve with a more refined grid. This is a consequence of the relatively high groove aspect ratio (length: 100 mm for a 0.7 mm × 0.7 mm cross-section), which implies a much greater number of elements along the longitudinal direction than in the transverse directions. .

4.1 Vapour Temperature

A common simplification in the evaporator models, i.e. [18] and references therein, is to consider that the vapour temperature in the groove is not significantly different from the saturation temperature. In order to assess the deviation from this assumption, a representative vapour temperature in the groove is extracted from the 3D field. This is performed considering the mixing temperature,

$$T_{mixing}(z) = \frac{\int_0^{Lxg}\int_{-Ly}^{-(Ly-Lyg)} T\|U\|dxdy}{U_{mixing(z)}} \tag{42}$$

where $U_{mixing}(z) = \int_0^{Lxg}\int_{-Ly}^{-(Ly-Lyg)}\|U\|dxdy$, $\|U\|$is the velocity norm. The axial variation of the mixing temperature is displayed in Fig.12.

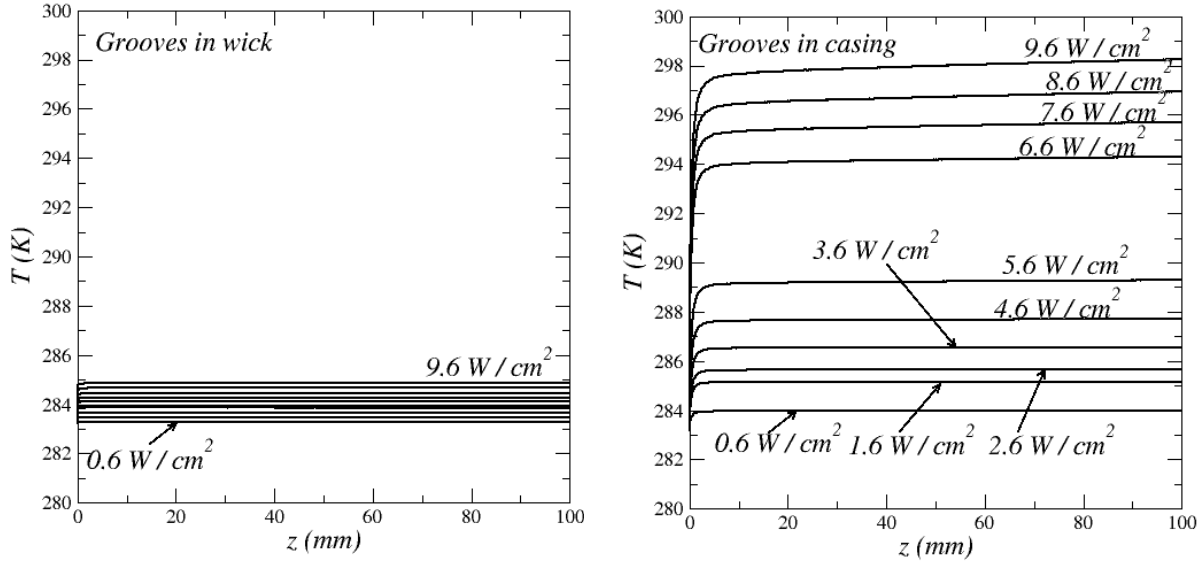

Fig. 12 - Variation of the mixing temperature along the groove for case of the grooves in the wick (left) and the case of the grooves in the casing case (right) for various heat fluxes.

As can be seen from Fig.12, the mixing temperature increases rapidly at the beginning of the groove and then varies little. The mixing temperature reaches 90 % of its maximum value (located at the groove outlet) after only 2 mm when the grooves are in the casing, consistently with the results reported in [27]. This short distance is significantly less (~0.25 mm) when the grooves are in the wick. When the grooves are in the wick, the mixing temperature remains relatively close to the saturation temperature imposed at the wick-groove interfacial surfaces. As illustrated in Fig.12 (left), the difference between the mixing temperature and the (wall) saturation temperature is less than 2K. The commonly used assumption that the temperature in the groove can be approximated by the saturation temperature is therefore reasonable in this case. By contrast, the mixing temperature is significantly greater than the saturation temperature when the grooves are in the casing. The difference is as high as about 15 K for the highest considered heat flux in Fig.12 and is significant even for a relatively low heat flux (~4-5 K for example for the heat flux of 5.6 W/cm^2). In this case, the commonly used procedure consisting in neglecting the vapour overheating in the groove is therefore questionable. The temperature variations in Figs.12 and 13 reflect the various regimes sketched in Fig.10 (for the case of the grooves in the casing, the transition between regimes I and II occurs at about 2 W/cm^2 and the transition between regime II and regime III occurs at about 6 W/cm^2). As shown in Fig.13, this difference between both cases is notably due to the temperature over the groove dead-end surface, which is significantly higher when the grooves are in the casing, i.e. closer to the maximum temperature located on top of the casing.

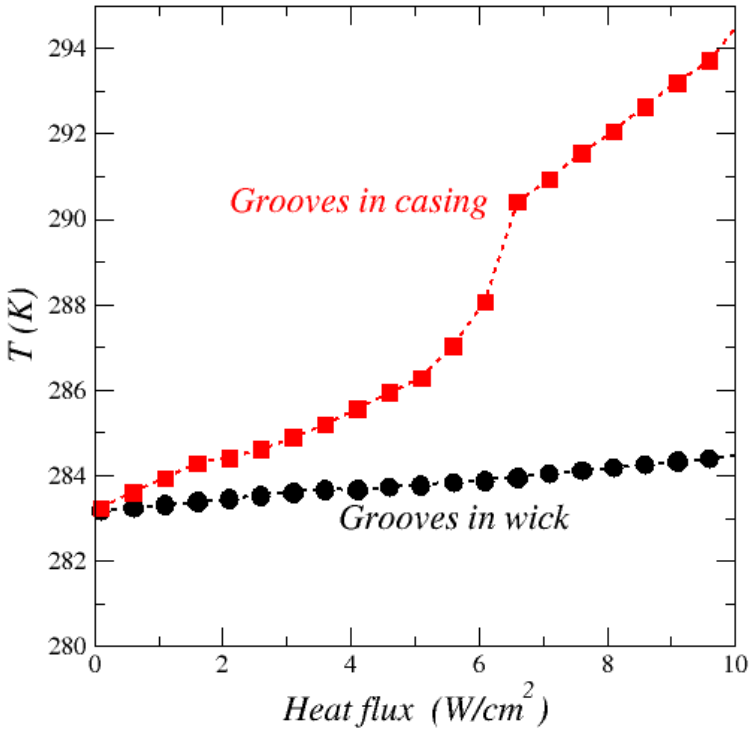

Fig. 13 - Average temperature on the groove end surface (see Figs.3 and 4) as a function of heat flux for the case of the groove in the wick and the case of the grooves in the casing.

The results show in Fig.14 further illustrate the fact that the temperature distribution is much more homogeneous in the groove when the groove is in the wick. By contrast, the temperature on the top surface of the groove becomes significantly higher than the groove mixing temperature when the groove is in the casing. In other words, there is a noticeable convective heat transfer between the casing and the groove due to the vapour flow in the wick when the grooves are in the casing since the temperature difference between the mixing temperature and the casing – groove top interface temperature is as high as 17 K for the highest considered heat flux.

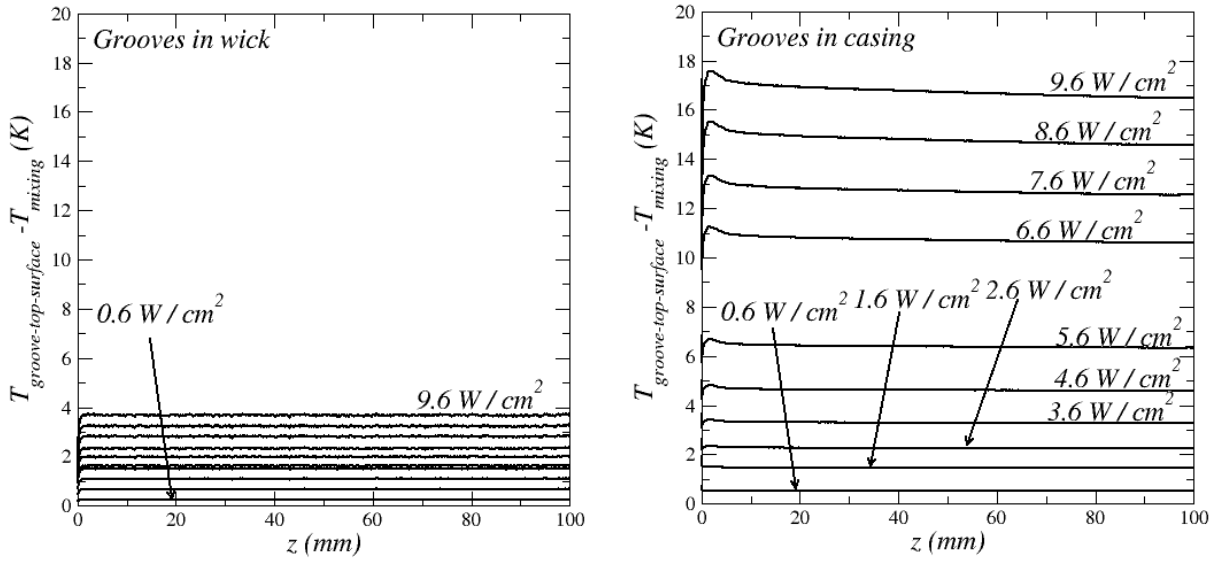

Fig.14 - Difference between the temperature on the groove top surface and the mixing temperature along the groove for various heat fluxes for the case of the grooves in the wick and the case of the grooves in the casing.

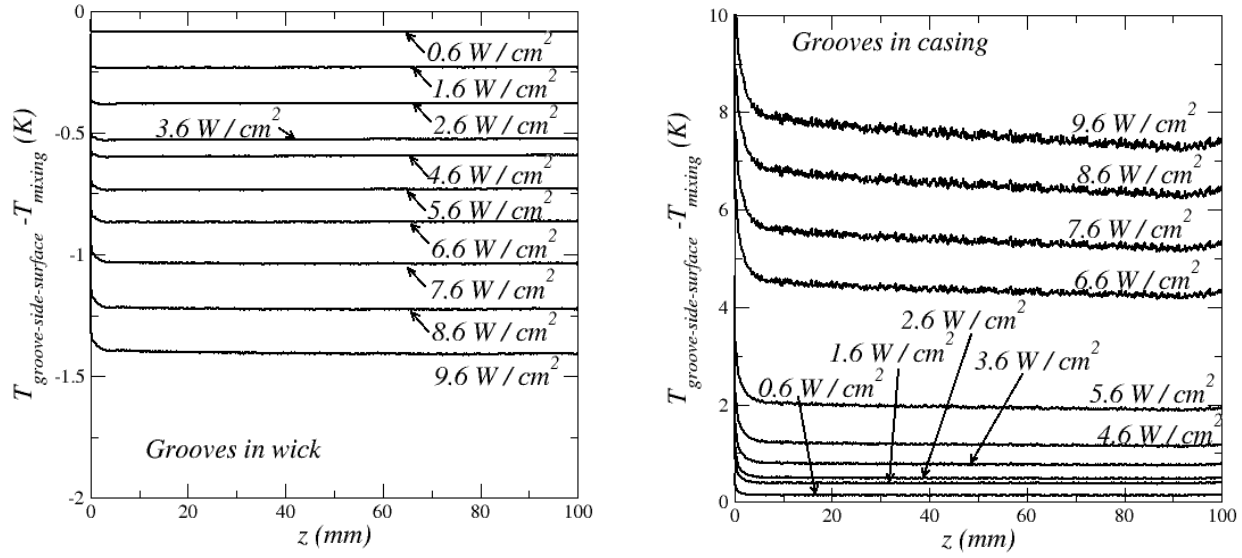

Fig.15 - Difference between the temperature on the groove side surface and the mixing temperature along the groove for various heat fluxes for the case of the grooves in the wick and the case of the grooves in the casing.

As depicted in Fig. 15, somewhat similar results are obtained as regards the difference between the groove side surface temperature and the mixing temperature. As can be seen, the mixing temperature is actually slightly greater than the wick surface temperature with the difference in temperature on the order 1-2 K when the grooves are in the wick. Although less than for the groove top surface, the temperature difference between the groove side surface temperature and the mixing temperature is significantly higher when the grooves are in the casing. For the highest considered flux, the mixing temperature is about 7-8 K lower than the casing side surface temperature.

Also two groups of curves can be distinguished in Fig. 15, as well as in Figs. 13 and 14, when the grooves are in the casing. There is a significant increase in the temperature difference when the heat flux is increased from 5.6 W/cm^2 to 6.6 W/cm^2. As for the temperature profiles depicted in Fig.8, the jump in the temperature difference can be related to the three main evaporator operating regimes sketched in Fig. 10. The temperature jump between the fluxes 5.6 W/cm^2 and 6.6 W/cm^2 in Figs. 13-15 corresponds to the transition between regime II and regime III when a vapour blanket starts forming in the wick.

4.2 Pressure drop

The axial velocity is continually increasing within the groove as a result of the uniform injection velocity at the wall. This is illustrated in Fig.16 where the variation of the Reynolds Number $\Re = \frac{\overline{U}_{vz}\rho_v D_H}{\mu_v}$ along the groove is plotted for both cases.

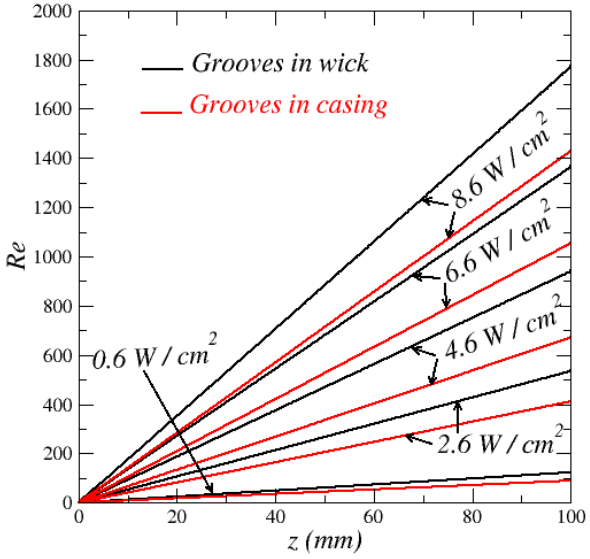

Fig.16 - Axial Reynolds number for the case of the grooves in the wick and the case of the grooves in the casing.

For the range of considered heat fluxes, the Reynolds number is always lower than 2500 which is the transition value between the laminar and turbulent regimes in a pipe. Although, the shape of the groove (different from a circular pipe) and the presence of the wall injection velocity should modify the value of the critical Reynolds number, assuming a laminar flow in the groove seems a quite reasonable assumption based on the results shown in Fig.16.

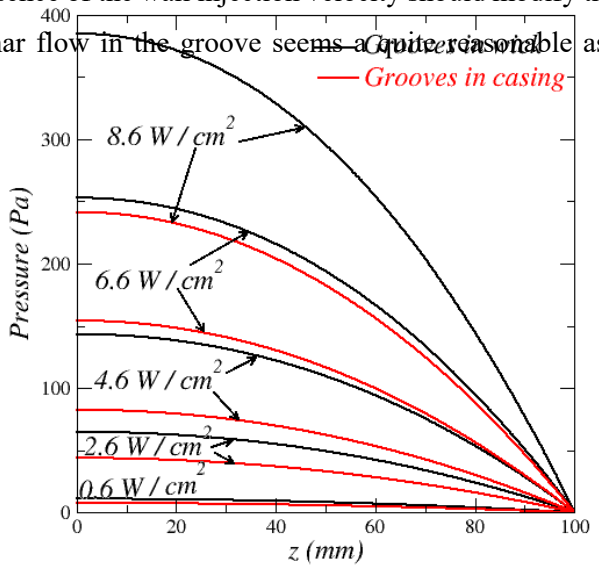

Fig.17 -Variation of groove cross-section averaged pressure in the groove for the cases of the grooves in the wick and in the casing.

The pressure in the groove is analysed through the consideration of the axial variation of the pressure averaged over the groove cross-section,

$$\overline{p}(z) = \frac{\int_0^{Lxg} \int_{-Ly}^{-(Ly-Lyg)} p dx dy}{L_{xg} L_{yg}} \tag{43}$$

As shown in Fig.17, the pressure varies non-linearly along the groove (note that the figure actually shows the difference $\overline{p}(z) - \overline{p}(z_{exit})$ where $\overline{p}(z_{exit})$ is the pressure at the groove exit). The parabolic shapes in Fig.17 are typical of a laminar flow with uniform injection velocity at the wall [28, 31].

The greater pressure drop for the case of the grooves in the wick compared to case of the grooves in the casing for the same heat flux is consistent with the comparatively higher velocities in Fig. 16 when the grooves are in the wick.

Also, it can be noticed that such pressure variations correspond to a quite small saturation temperature variations (0.02 K for the highest considered flux) according the Clausius-Clapeyron relationship. In this

respect, neglecting the impact of the pressure variation within the groove on the saturation temperature is a quite reasonable assumption.

4.3 Heat transfer coefficient

As illustrated in Fig.16, the axial velocity starts from a null value and increases continually along the groove. Thus, the heat transfer is by conduction at the beginning of the groove. Then when the velocity increases the importance of heat transfer by forced convection becomes important. This can be characterized by the Peclet number $Pe = \Re Pr$, where *Pr* is the Prandtl number comparing the significance of convective and conductive heat transfers. Since the Prandtl number for ammonia is closed to 1 (*Pr* = 1.12), the variations of the Peclet number are actually very similar to the ones of the Reynolds number depicted in Fig. 16. As can be seen from Fig.16, the convective heat transfer becomes very rapidly dominant. In other words, the extension of the zone where the heat conduction is on the same order as the convective heat transfer is quite small for both cases (< 0.25 mm).

The heat transfer within the groove is characterized from the computation of heat transfer coefficients defined using a classical Newton's law formulation. The heat transfer coefficient along the groove top surface is computed as

$$h_{top}(z) = \left| \frac{\overline{\varphi}_{top}(z)}{T_{mixing}(z) - \overline{T}_{top}(z)} \right| \tag{44}$$

where $\overline{\varphi}_{top}(z)$ is the average heat flux along the *x* direction at the *z* position over the groove top surface (groove-casing top interface),

$$\overline{\varphi}_{top}(z) = \frac{1}{L_{xg}} \int_0^{L_{xg}} (-\lambda_v \nabla T.n) dx \tag{45}$$

and $\overline{T}_{top}(z)$ is the average temperature along the *x* direction at the *z* position over the groove top surface

$$\overline{T}_{top}(z) = \frac{1}{L_{xg}} \int_0^{L_{xg}} T dx \tag{46}$$

Similarly, the heat transfer coefficient at the casing-groove vertical interfacial surface (for the case of the grooves in the casing) is defined as

$$h_{side}(z) = \left| \frac{\overline{\varphi}_{side}(z)}{T_{mixing}(z) - \overline{T}_{side}(z)} \right| \tag{47}$$

where

$$\overline{\varphi}_{side}(z) = \frac{1}{L_{yg}} \int_{-L_y}^{-(L_y - L_{yg})} (-\lambda_v \nabla T.n) dy \tag{48}$$

and

$$\overline{T}_{side}(z) = \frac{1}{L_{yg}} \int_{-L_y}^{-(L_y - L_{yg})} T dx \tag{49}$$

For the case of the grooves in the wick, the side surface (surface #6 in Fig.3) is a wick-groove interfacial surface. Therefore, the heat transfer at the wall also depends on the blowing effect associated with the injection velocity resulting from the vaporization. However, the average injection velocity over this surface is much smaller than the axial velocity, which leads to a small wall Peclet number. For this reason, the convective heat transfer associated with the injection velocity was computed using the same convention as for the casing solid surface, that is from equations similar to Eqs.(46-47). For the same reason, the heat transfer coefficient at the groove bottom surface was computed as

$$h_{bottom}(z) = \left| \frac{\overline{\varphi}_{bottom}(z)}{T_{mixing}(z) - \overline{T}_{bottom}(z)} \right| \tag{50}$$

$$\overline{\varphi}_{bottom}(z) = \frac{1}{L_{xg}} \int_0^{L_{xg}} (-\lambda_v \nabla T.n) dx \tag{51}$$

$$\overline{T}_{bottom}(z) = \frac{1}{L_{xg}} \int_0^{L_{xg}} T dx \tag{52}$$

The variations of the above defined heat transfer coefficients along the groove are depicted in Figs. 18-20 for both cases. As can be seen, the curves are noisy with noticeable longitudinal fluctuations (dotted lines in Figs. 18-20). As the convective coefficient is computed from the division of the mean heat flux by the average temperature difference, a small variation in the temperatures can lead to a noticeable variation of the coefficient. Note for instance that, as shown in Fig.17, the temperature difference for the case of the grooves in the wick is quite small. Thus a small inaccuracy in the temperature differences between two successive mesh points along the groove can cause fluctuations. Also as depicted in Figs.10-11, the injection velocities at the wick-groove interfaces vary significantly. This can be a source of fluctuations with a too coarse grid. The fluctuations were reduced by increasing the mesh fineness. However, when the mesh fineness was too large, the computation could not converge. The results depicted in Figs.18-20 represent the best trade-off we could obtain between mesh-fineness and convergence. In other words, the fluctuations can be attributed to a lack of mesh refinement. In order to obtain a clearer view of the heat transfer coefficient behaviour, the fluctuations were smoothed out by using a running average procedure. This led to the solid lines shown in Figs 18-20. As can be seen, these lines show clear and consistent trends. Although performing the simulations over a more

refined mesh remains desirable, it is our belief that the results should be very similar to the ones depicted in Fig.18-20.

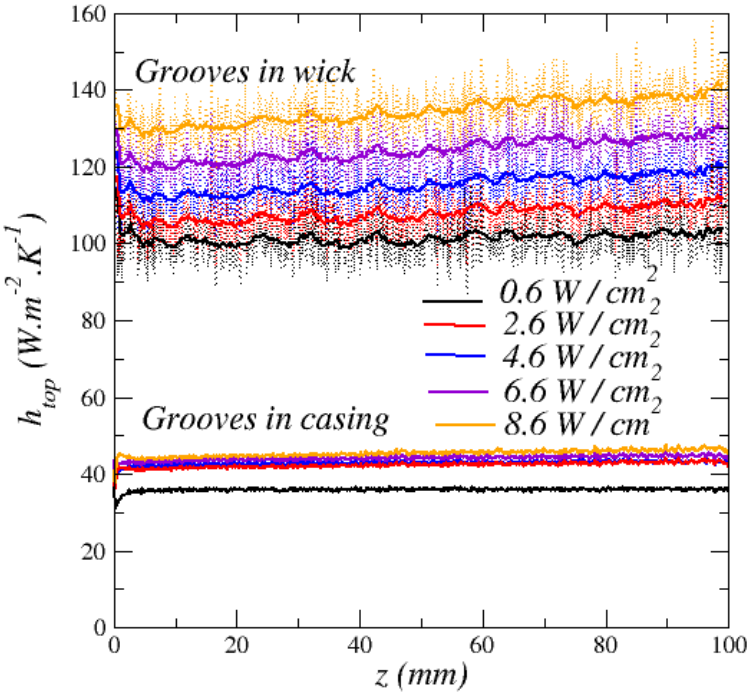

Fig.18. Groove top limiting surface heat transfer coefficient for the cases of the grooves in the wick and in the casing. The solid lines represent running averages over 50 successive points along the groove.

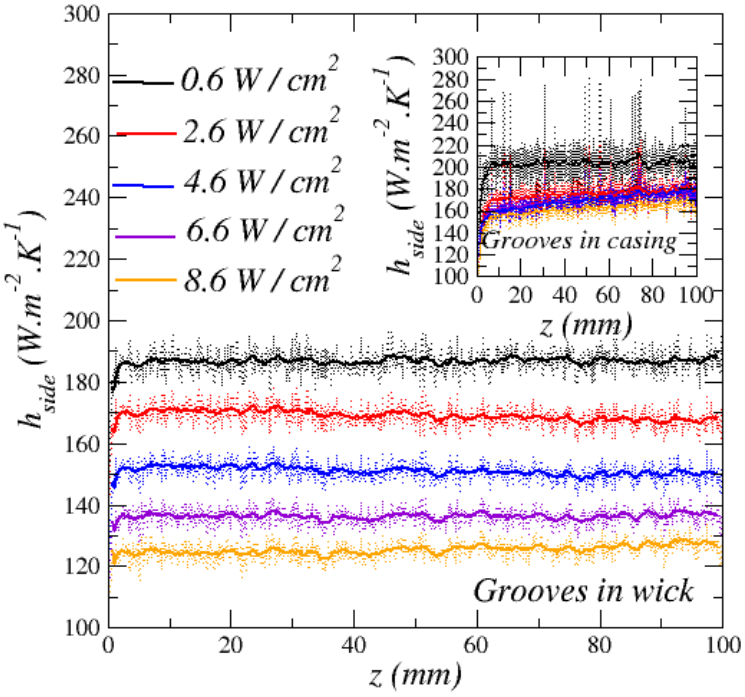

Fig.19 - Groove side limiting surface heat transfer coefficient for the cases of the grooves in the wick in the casing. The solid lines represent running averages over 50 successive points along the groove.

As can be seen, various behaviours can be observed depending on the considered case and the considered surface. For a given flux, the heat transfer coefficient can be almost constant outside the region at the beginning of the groove for some surfaces. Otherwise, the trend is a slight increase along the groove.An exception is the coefficient for the groove bottom limiting surface for the case of the grooves in the wick. As illustrated in Fig. 20 left, this heat transfer coefficient decreases along the groove in qualitative agreement with the behaviour reported in [28] for the simpler case of a duct with one wall subjected to uniform injection and constant heat flux

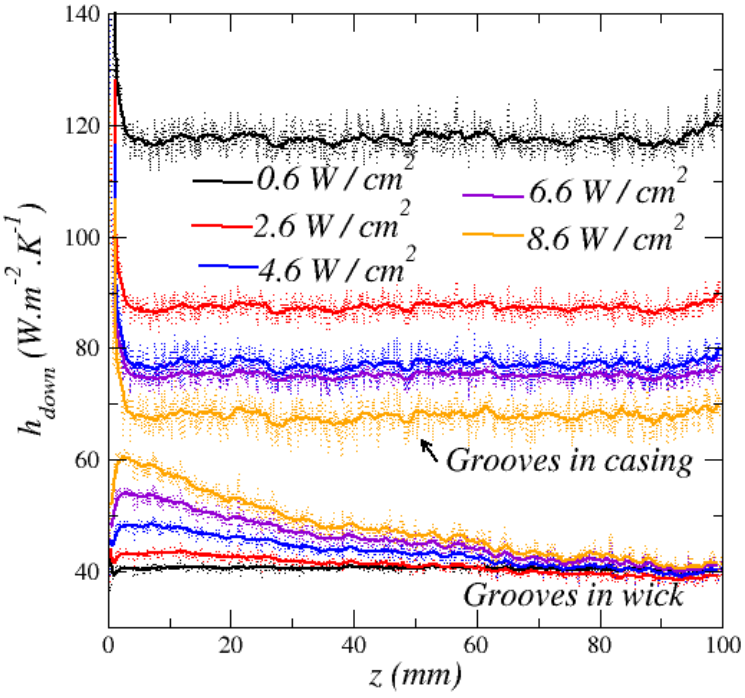

Fig.20 - Groove bottom limiting surface heat transfer coefficient for the cases of the grooves in the wick and in the casing. The solid lines represent running averages over 50 successive points along the groove.

For the sake of comparison, Fig.21 shows the variation of the heat transfer coefficient computed using Eq.(35), i.e. a classical correlation [25]. Contrary to our results, this correlation predicts a noticeable increase in the coefficient along the groove. In addition to a different spatial variation, the coefficient values are also quite different. The correlation significantly overestimates the coefficients compared to our simulation results. It can

be argued that this correlation has been developed for turbulent flows whereas our simulations indicate a laminar flow. However, all the commonly used correlations of the literature for the convective heat transfer in pipes, e.g. [32], predict an increase of the heat transfer coefficient with the velocity.

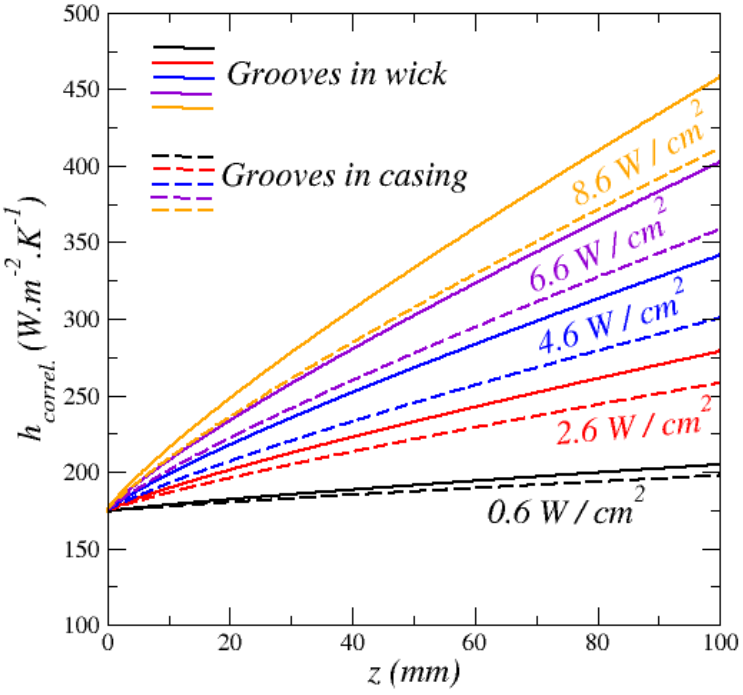

Fig.21 - Heat transfer coefficient computed using the classical correlation Eq.(35) for the cases of the grooves in the wick and in the casing .

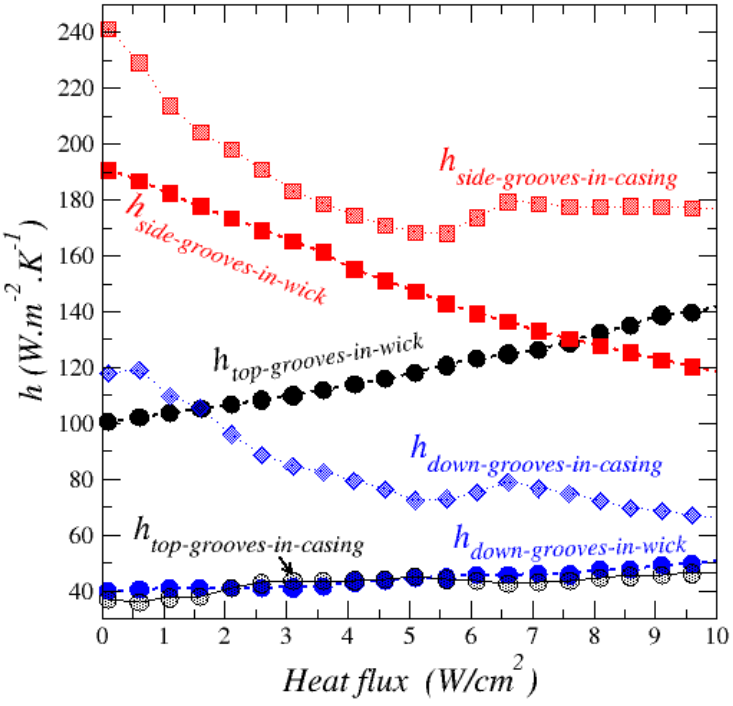

Fig.22 - Mean heat transfer coefficient over the various groove limiting surfaces for the cases of the grooves in the wick and in the casing.

An important feature illustrated in Figs.14 and 15 lies in the fact that the temperature varies from one limiting surface to the other. In other words, the assumption of a similar wall temperature on the two casing-groove interfacial surfaces in the case of the grooves in the casing, as considered for instance in [27], is not correct. This variability between the groove limiting surfaces can also be seen with the heat transfer coefficients and is further illustrated in Fig. 22 showing the variation of the mean heat transfer coefficient for the various surfaces for both cases.

5. Discussion

The results presented in Section 4 indicate that the coupling between the transfer in the grooves and the transfer in the other elements of the evaporator (casing, wick, etc) must be improved since most models of the literature are based on questionable assumptions and make use of questionable heat transfer coefficient correlations. However, it can be noticed that the PNM simulations themselves, which were used to generate the boundary conditions for the groove COMSOL simulations (as sketched in Fig.5) imply to take into account the heat and mass transfer in the groove. As explained in section 3, this was performed using a simplified approach. In that sense, the coupling between the COMSOL simulations and the PNM simulations used in the present study can be seen as a one-way coupling. In other words, the results of the COMSOL simulations were not taken into account to possibly improve the PNM simulations. Thus, still more accurate results can be expected through an iterative procedure between the evaporator PNM simulations and the groove COMSOL simulations (for instance by using the convective heat transfer coefficient determined from the COMSOL simulations in the PNM simulations). This is left for a future work. It can be noticed, however, that such a two-way coupling approach would be quite computationally demanding. Also, contrary to the COMSOL simulations, the PNM simulations did not take into account the groove dead-end region where the groove is closed by the casing. The PNM computational domain corresponds to a region of the evaporator away from this region. In spite of these shortcomings, we believe that the one way coupling method used in the present study and the associated results are a step forward bringing interesting results on the heat and mass transfer in the evaporator grooves.

6. Conclusion

Three-dimensional simulations of the convective heat transfer inside the vapour removal channels (grooves) of a LHP evaporator were performed for two channel configurations: when the channels are in the wick and

when the channels are in the casing. The boundary conditions were imported from simulations based on a discrete pore network representation of the wick referred to as a pore network model (PNM).

The results show significant differences between the two cases and also with commonly made assumptions. When the groove is in the wick, the commonly used assumption that the vapour temperature is close to the saturation temperature is acceptable. This assumption is not valid anymore when the groove is in the casing. A significant vapour overheating is obtained (up to 10 K). However, the assumption of a constant vapour temperature within the groove is acceptable for both cases except in a short region at the very beginning of the groove.

The study of the pressure drop along the groove confirms that the assumption of a constant saturation temperature within the groove is acceptable since the pressure variation along the groove remains small compared to the mean pressure in the groove.

The temperature varies from one limiting surface of the groove to the other for a given heat flux. This is also the case as regards the heat transfer coefficient. Also, this coefficient was found to be almost constant or varying only slightly along the groove over several of the groove limiting surfaces for a given heat flux. This is contrast with the commonly used correlations of heat transfer in pipes in the absence of injection which all predicts an increase of the Nusselt number with the Reynolds number. Contrary to the classical situation where the velocity is constant within the pipe, the fluid velocity increases continuously in an evaporator groove as the result of the vaporisation along the evaporator. This has a great impact on the heat transfer coefficient behaviour, which is thus markedly different from the behaviour in pipes without wall injection.

In summary, the present study indicates that the coupling between the transfer in the grooves and the transfer in the other elements of the evaporator (casing, wick, etc) must be improved since most models are based on questionable assumptions and make use of questionable heat transfer coefficient correlations.

Acknowledgments

The financial supports from CNES and Airbus Defence and Space are gratefully acknowledged.

References

1. V. Ayel, L. Lachassagne, Y. Bertin, C. Romestant Experimental Analysis of a Capillary Pumped Loop for Terrestrial Application, J. of Thermophysics and Heat Transfer 25 (4) (2011) 561-571.
2. L. Lachassagne, V. Ayel, C. Romestant, Y. Bertin, Experimental study of capillary pumped loop for integrated power in gravity field, Appl. Therm. Eng., 35 (2012) 166-176.
3. L.Lachassagne,Y.Bertin,V.Ayel, C.Romestant, Steady-state modeling of Capillary Pumped Loop in gravity field, International Journal of Thermal Sciences, 64 (2013) 62-80.

4. F. Accorinti, V. Ayel, Y. Bertin, Steady-state analysis of a Capillary Pumped Loop for Terrestrial Application with methanol and ethanol as working fluids, International Journal of Thermal Sciences, 137 (2019) 571-583.
5. M.Nikitkin, B.Cullimore, CPL and LHP Technologies: What are the Differences, What are the Similarities? Journal of Aerospace, SAE Transactions, 107 (1) (1998) 400-408.
6. K Nakamura, K Odagiri, H Nagano, Study on a loop heat pipe for a long-distance heat transport under anti-gravity condition, Applied Thermal Engineering, 107 (2016) 167-174.
7. M Nishikawara, H Nagano, Numerical simulation of capillary evaporator with microgap in a loop heat pipe, International Journal of Thermal Sciences, 102 (2016) 39-46, 2016
8. R Boubaker, V Platel, S Harmand, A numerical comparative study of the effect of working fluids and wick properties on the performance of capillary pumped loop with a flat evaporator, Applied Thermal Engineering, 100 (2016) 564-576.
9. M Nishikawara, H Nagano, M Prat, Numerical study on heat-transfer characteristics of loop heat pipe evaporator using three-dimensional pore network model, Applied Thermal Engineering, 126 (2017) 1098-1106.
10. R. Giraudon, S. Lips,D. Fabregue, L. Gremillard, E. Maire, V. Sartre, Design, manufacturing, and characterization of copper capillary structures for loop heat pipes, Heat Pipe Science and Technology, An International Journal, 8(1) (2017), 27-49.
11. AR Anand, A Jaiswal, A Ambirajan, P Dutta, Experimental studies on a miniature loop heat pipe with flat evaporator with various working fluids, Applied Thermal Engineering, 144 (2018) 495-503.
12. R Boubaker, S Harmand, V Platel, Experimental study of the liquid/vapour phase change in a porous media of two-phase heat transfer devices, Applied Thermal Engineering, 143 (2018) 275-282.
13. M Nishikawara, Y Ueda, H Yanada, Static and dynamic liquid-vapour phase distribution in the capillary evaporator of a loop heat pipe, Microgravity Science and Technology, 31 (2019) 61–71.
14. K Odagiri, H Nagano, Investigation on liquid-vapour interface behavior in capillary evaporator for high heat flux loop heat pipe, International Journal of Thermal Sciences, 140 (2019) 530-538.
15. AR Anand, A Ambirajan, P Dutta, Investigations on vapour blanket formation inside capillary wick of loop heat pipe, International Journal of Heat and Mass Transfer, 156 (2020) 119685.
16. S Launay, V Sartre, J Bonjour, Parametric analysis of loop heat pipe operation: a literature review,International Journal of Thermal Sciences, 46 (7) (2007) 621-636.
17. Y. Maydanik, M. Chernysheva, V. Pastukhov, Review: loop heat pipes with flat evaporators, Appl. Therm. Eng., 67 (2014) 294-307.
18. L. Mottet, T. Coquard, and M. Prat, Three-dimensional liquid and vapour distribution in the wick of capillary evaporators, Int. J. Heat Mass Transf., 83 (2015) 636–651.
19. J. Ku, Operating Characteristics of Loop Heat Pipes, 29 th Int. Conf. Environ. Syst., p. 16, 1999.

20. S. Launay, V. Platel, S. Dutour, and J.-L. Joly, Transient Modeling of Loop Heat Pipes for the Oscillating Behavior Study, J. Thermophys. Heat Transf. 21(3) (2007) 487–495.
21. T. Adachi, K. Fujita, and H. Nagai, Numerical study of temperature oscillation in loop heat pipe, Appl. Therm. Eng., 163 (2019) 114281.
22. Y Cao, A Faghri, Conjugate analysis of a flat-plate type evaporator for capillary pumped loops with three-dimensional vapour flow in the groove, International Journal of Heat and Mass Transfer, 37(3) (1994) 401-409. 19
23. J. Li and G. P. Peterson, 3D heat transfer analysis in a loop heat pipe evaporator with a fully saturated wick, Int. J. Heat Mass Transf., 54 (1-3) (2011) 564–574.
24. M Nishikawara, H Nagano, L Mottet, M Prat, Formation of unsaturated regions in the porous wick of a capillary evaporator, International Journal of Heat and Mass Transfer, 89 (2015) 588-595.
25. .A. Sleicher, M. Rouse, A convenient correlation for heat transfer to constant and variable property fluids in turbulent pipe flow, Int. J. Heat Mass Transfer 18 (5) (1975) 677–683.
26. T. Kaya and J. Goldak, Numerical analysis of heat and mass transfer in the capillary structure of a loop heat pipe," International Journal of Heat and Mass Transfer, 49 (2006) 3211-3220.
27. N. Jesuthasan, Modeling of Thermofluid Phenomena in Segmented Network Simulations of Loop Heat Pipes, Ph.D thesis, McGill University (2011).
28. G.J.Hwang, Y.C.Cheng and M.L.Ng, Developing laminar flow and heat transfer in a square duct with one-walled injection and suction, Int. J. Heat Mass Transfer 36 (9) (1993) 2429-2440.
29. J.Yuan, M.Rokni, B.Sundén, Simulation of fully developed laminar heat and mass transfer in fuel cell ducts with different cross-sections, Int. J. Heat Mass Transfer, 44 (21) (2001) 4047-4058.
30. A. Attari Moghaddam, A Kharaghani, E Tsotsas, M Prat, Kinematics in a slowly drying porous medium: Reconciliation of pore network simulations and continuum modeling, Physics of fluids 29 (2) (2017) 022102.
31. R.M. Terrill, P.W. Thomas, On laminar flow through a uniformly porous pipe, Applied Scientific Research, 21 (1969) 37-67,
32. TL Bergman, FP Incropera, DP DeWitt, AS Lavine, Fundamentals of heat and mass transfer, Wiley (2011).